



# Counterstreaming Strahls and Heat Flux Dropouts as Possible Signatures of Local Particle Acceleration in the Solar Wind

O. Khabarova<sup>1</sup> , V. Zharkova<sup>2</sup> , Q. Xia<sup>2</sup> , and O. E. Malandraki<sup>3</sup> <sup>1</sup> Heliophysical Laboratory, Pushkov Institute of Terrestrial Magnetism, Ionosphere and Radiowave Propagation of the Russian Academy of Sciences (IZMIRAN), Troitsk, Moscow 108840, Russia; [khabarova@izmiran.ru](mailto:khabarova@izmiran.ru)<sup>2</sup> Northumbria University, Newcastle, UK<sup>3</sup> IAASARS, National Observatory of Athens, Penteli, Greece

Received 2020 January 19; revised 2020 February 26; accepted 2020 March 7; published 2020 May 5

## Abstract

Suprathermal electrons with energies of  $\sim 70$  eV and above are observed at 1 au as dispersionless halo electrons and magnetic field-aligned beams of strahls. For a long time, it has been thought that both populations originate only from the solar corona, and that the only active process impacting their properties in the solar wind is scattering. This view has consequently impacted the interpretation of typical patterns of pitch-angle distributions (PADs) of suprathermal electrons. Meanwhile, recent observational studies supported by numerical simulations have shown that there is an unaccounted population of electrons accelerated to suprathermal energies at reconnecting current sheets (RCSs) and 3D dynamical plasmoids (or 2D magnetic islands (MIs)) directly in the heliosphere. We present multispacecraft observations of counterstreaming strahls and heat flux dropouts in PADs within a region filled with plasmoids and RCSs unaffected by interplanetary shocks, comparing observed PAD features with those predicted by particle-in-cell simulations. We show typical PAD patterns determined by local acceleration of thermal-core electrons up to hundreds of electron volts. Resulting PAD views depend on properties and topology of particular RCSs, MIs, and plasma/magnetic field parameters. Our study suggests that solar wind-borne suprathermal electrons coexist with those of solar origin. Therefore, some of heat flux dropout and bidirectional strahl events can be explained by local dynamical processes involving magnetic reconnection. Possible implications of the results for the interpretation of the actively debated decrease in the strahl/halo relative density with heliocentric distance and puzzling features of suprathermal electrons observed at crossings of the heliospheric current sheet and cometary comas are also discussed.

*Unified Astronomy Thesaurus concepts:* [Interplanetary magnetic fields \(824\)](#); [Solar magnetic reconnection \(1504\)](#); [Solar wind \(1534\)](#); [Solar energetic particles \(1491\)](#); [Interplanetary particle acceleration \(826\)](#)

## 1. Introduction

The dynamics of suprathermal electrons with energies above the Maxwellian thermal core (usually  $>50$  eV at 1 au), comprising of (i) isotropic or weakly anisotropic halo, and (ii) strahl (or beam) electrons aligned with the magnetic field, is often used for diagnostics of the topology of the interplanetary magnetic field (IMF; e.g., Crooker et al. 2004; Gosling et al. 2006; Owens et al. 2013). Pitch-angle distribution (PAD) spectrograms of suprathermal electrons represent a tool that helps reveal the dominant IMF direction using strahl properties. In the solar wind, strahl beams are seen in PADs as stripes of the red/yellow color (corresponding to the maximum flux intensity) located near  $0^\circ$  or  $180^\circ$ , thus, indicating the dominant IMF direction either away or toward the source of suprathermal electrons. The latter is predominantly supposed to be the solar corona (e.g., Vocks et al. 2005; Štverák et al. 2009; Anderson et al. 2012; Graham et al. 2017; Horaites et al. 2019). PAD patterns help identify the heliospheric current sheet (HCS) crossings or other changes in the global IMF configuration like crossings of borders of high-speed streams/flows in the solar wind (e.g., Crooker et al. 2004; Gosling et al. 2006; Simunac et al. 2012).

In the simplest case of the IMF sector boundary crossing, a PAD profile should demonstrate the quick disappearance of one stripe and the appearance of the other while the IMF polarity changes (e.g., Gosling et al. 2006). However, this ideal picture is rarely observed. Instead, the PADs often show specific and widely discussed features, namely, defocused beams called heat flux dropouts, dispersionless vertical patterns, signatures of the unstable direction of strahls, and so-called bidirectional (or counterstreaming) strahls (McComas et al. 1989; Crooker et al. 2004; Pagel et al. 2005; Crooker & Pagel 2008; Foullon et al. 2009; Simunac et al. 2012; Kajdič et al. 2013).

The earlier attempts to interpret the strange PAD effects considered only those scenarios involving the magnetic field lines connected to the Sun. Thus, the occurrence of counterstreaming strahls, i.e., two stripes observed in the PADs at both  $0^\circ$  and  $180^\circ$ , was interpreted as a signature of a direct connection of the point of observations to the sources of hot electrons rooted in the corona at the two edges of a closed, loop-like magnetic field line (e.g., Gosling et al. 1987; McComas et al. 1989). Explanations of the dropouts and (sometimes) bidirectional strahls through the occurrence of large-scale loops detached from a single reconnection null point in the solar wind and moving back to the Sun or by entangling and bending of the whole HCS backward to the Sun have been very popular for decades (e.g., Crooker et al. 2004; Foullon et al. 2009; Rouillard et al. 2010).



Original content from this work may be used under the terms of the [Creative Commons Attribution 4.0 licence](#). Any further distribution of this work must maintain attribution to the author(s) and the title of the work, journal citation and DOI.

Although possible local effects like magnetic reconnection were also suggested (e.g., Crooker & Pagel 2008; Foullon et al. 2009), the dominant paradigm did not take local structures and local particle acceleration into account. It has been believed that current sheets (CSs) formed in the heliosphere are large in width and thus can reconnect only slowly, not accelerating particles efficiently. On the other hand, efficient mechanisms of local particle acceleration suggesting stochastic magnetic reconnection have been known too (Matthaeus et al. 1984; Drake et al. 2009; Zank et al. 2014, 2015; Eyink 2015; le Roux et al. 2015, 2016, 2018; Le Roux et al. 2019; Li et al. 2019; Lazarian et al. 2020). Consequently, the paradigm of large, planar, and passive CSs that cannot accelerate particles and bend or fold back in the heliosphere under a single act of magnetic reconnection has become actively debated.

Recent solar wind observations and theoretical simulations (Zharkova & Khabarova 2012, 2015; Egedal et al. 2015; Khabarova et al. 2015, 2016, 2018; Uzdensky & Loureiro 2016; Khabarova & Zank 2017; Xia & Zharkova 2018, 2020; Adhikari et al. 2019; Malandraki et al. 2019; Mingalev et al. 2019) revealed that (i) reconnecting current sheets (RCSs) are often subject to instabilities breaking those into 3D small-scale plasmoids/blobs or 2D magnetic islands (MIs) with multiple X- and O-nullpoints; (ii) RCSs and dynamical MIs can accelerate particles up to the MeV/nuc energies; (iii) accelerated particles may form clouds expanding far from a reconnecting region; and (iv) bidirectional strahls observed in PADs may simply represent a signature of reconnection occurring at closed IMF structures (e.g., MIs), not necessarily connected to the Sun.

In this study, we show multispacecraft observations of suprathermal electrons in a region filled with CSs and MIs and compare the observed PAD features with theoretical predictions made for similar IMF/plasma configurations, using particle-in-cell (PIC) approaches proposed by Xia & Zharkova (2018, 2020).

## 2. Observations

We have selected the event previously discussed in Khabarova et al. (2016) as a clear case of particle acceleration in dynamical MIs not impacted by high-speed streams/flows. An interaction of a coronal hole flow with a weak coronal mass ejection led to the formation of a giant swirl in the solar corona, which propagated, rotating, far away from the Sun. As a result, in 2007 May 28–31, the Earth and all near-Earth spacecraft (STEREO A, STEREO B, Wind, and ACE) appeared inside the magnetic cavity filled with MIs representing remnants of the swirl. Khabarova et al. (2016) investigated in detail the interplanetary conditions and analyzed observations of key IMF and plasma parameters from STEREO A for this event, identifying MIs and showing the energetic ion flux increase in the magnetic cavity. Figure 1 shows the corresponding observations of the key solar wind parameters at  $\sim 1$  au. The stream interaction region (SIR) was detected by the L1 spacecraft (Figure 1(a)) practically simultaneously with STEREO A (Figure 1(b)), and then the plasma reached STEREO B (Figure 1(b)). This feature indicates a strong twist of the SIR front with respect to the Parker spiral, since normally it is observed by STEREO B first (Gómez-Herrero et al. 2011). The MI-containing region observed on 2007 May 28–31 was characterized by very similar profiles of the key parameters detected by all the spacecraft with an unusually

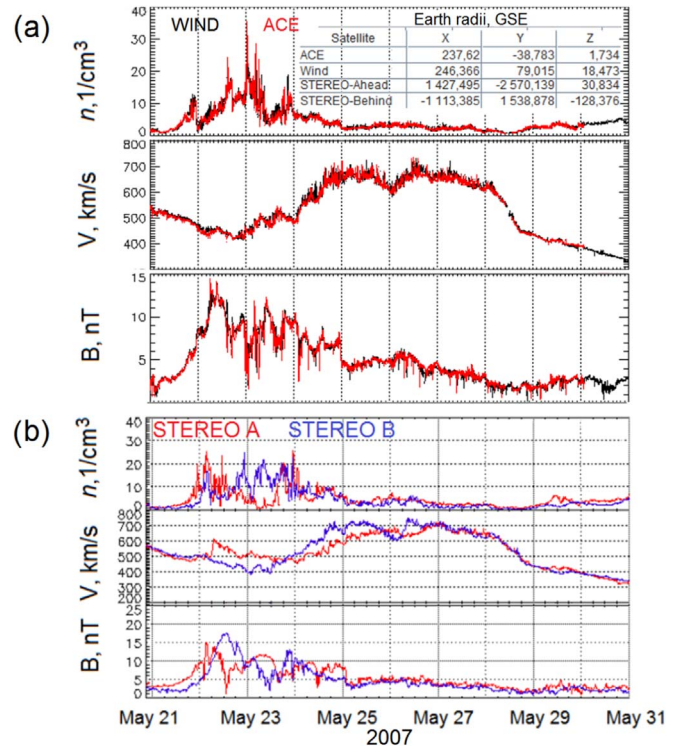


**Figure 1.** Observations of key solar wind parameters by different spacecraft during the passage of the SIR interrupted by the swirl shown in Figure 8 of Khabarova et al. (2016). Most of MIs are observed inside the remnants of the swirl on 2007 May 28–31. Three panels in (a) and (b) from top to bottom are the solar wind density, the solar wind speed, and the IMF strength obtained from the L1 (ACE and WIND) spacecraft (a) and the STEREO A and STEREO B spacecraft (b). The MI-containing region is characterized by very similar profiles of all the parameters observed by the spacecraft with an unusually minimal time-shift. ACE and WIND observations are practically identical, but since ACE have some data gaps, we will use below the WIND measurements to analyze how electrons of different energies behave at crossings of MIs.

minimal time-shift. Therefore, plasma samples under current study from the center of the region (2007 May 29) correspond to the same samples as analyzed in Khabarova et al. (2016).

The upper five panels in Figure 2 represent measurements of PADs of suprathermal electrons from the electron electrostatic analyzer (EESA-low), which is a part of the WIND 3DP instrument (<http://sprg.ssl.berkeley.edu/wind3dp/>). The energies range from middle  $\sim 540$  eV of undoubtedly suprathermal electrons to low  $\sim 29$  eV of electrons at the edge between the core and halo electron populations (mainly core). The electron total flux intensities are given by color. MIs can be seen in Figure 2 as intense anticorrelated variations in the IMF components, not stochastic as usually seen in simple turbulent regions, but appearing as humps of approximately an hour in length (more about signatures of MIs can be found in Khabarova et al. 2015, 2016; Khabarova & Zank 2017). The vertical dashed lines indicate borders of MIs, and each border represents a current sheet. Analyzing the lower (black and white) panels of Figure 2 with IMF and density parameters, one can note that the MIs with the largest IMF strength and the slightly elevated density are observed from  $\sim 8$  UT. Such conditions lead to intensification of magnetic reconnection in the region. The largest MIs are observed from 13 UT to 22 UT. Overall, the IMF patterns show the presence of smaller-scale dynamic MIs in the left part of Figure 2, the main reconnecting

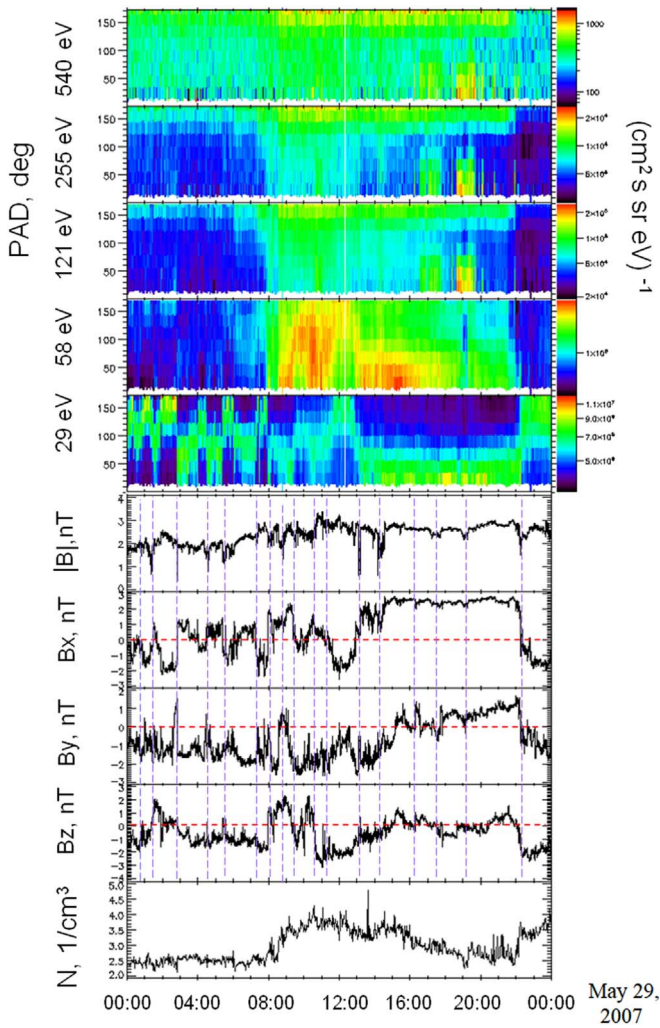


**Figure 2.** Behavior of electrons of different energies, the IMF, and the density in the region filled with MIs of variable size as observed by the WIND spacecraft on 2007 May 29. From top to bottom: PADs of electrons measured with  $\sim 24$  s resolution in the following channels: Channel 3 (often  $\sim 540$  eV); Channel 5 (often  $\sim 255$  eV); Channel 7 (often  $\sim 121$  eV); Channel 9 (often  $\sim 58$  eV); Channel 11 (often  $\sim 29$  eV); the IMF strength; the three IMF components in the GSE system; and the solar wind density. Crossings of CSs separating MIs are shown by vertical dashed purple lines.

relatively large MIs in the middle, and the larger but more stable MIs in the right part.

The first noteworthy feature is that electrons of different energies behave differently. It is known that usually PAD patterns vary rather slowly from channel to channel even in the disturbed solar wind (e.g., see Kajdič et al. 2013 and Figure 11 of Khabarova et al. 2016), but in this case, the following different features are seen in different channels in Figure 2:

1. Electrons in the lowest energy 11 channel closely follow the magnetic topology of smallest and dynamical MIs (see the up-and-down variations occurring in accordance with most intense variations in the IMF).
2. The PAD of channel 9 shows a dramatic change in the behavior of electrons in comparison with lower-energy electrons. Electrons do not orbit the MIs, and the direction of the electron motion shows a clear anticorrelation of variations of pitch angles with respect to the patterns seen in higher-energy channels 7 and 5. Furthermore, the most intense flux follows the position

of the most intensely reconnecting MIs in the middle of Figure 2 (compare the bird-like red PAD pattern and large-scale variations in  $B_x$ ).

3. The channel 5 PAD indicates uninterrupted/smooth strahl flowing in the sunward direction (the color stripe at the top of the PAD in the left part of the panel) until the approach to the region of the strongest and largest reconnecting MIs in the middle of Figure 2. From  $\sim 8$  UT, the intense dispersionless vertical feature is seen in the 5–9 channel PADs (green vertical region), and in the area of large and rather undisturbed MIs there are features of bidirectionality seen in the higher-energy 3–7 channel PADs. The PAD for channel 5 looks similar to channel 7.
4. The PAD of suprathermal electrons in channel 3 shows signatures of counterstreaming strahls (red and yellow stripes at  $0^\circ$  and  $180^\circ$ ) in the background of the intense dispersionless halo (green).

Observations of higher-energy electrons with the EESA-high instrument were not at as good a level as those provided by EESA-low, which are shown in Figure 2, and higher-energy PAD features were poorly recognizable. Fortunately, obtaining the IMPACT/MAG Magnetic Field and PLASTIC Solar Wind Plasma data from the other spacecraft, the STEREO pair (<http://sprg.ssl.berkeley.edu/impact/>), allows us to extend the study up to higher possible energies, comparing the available STEREO measurements of the energetic electron direction with WIND observations.

The behavior of suprathermal electrons in both the lower PAD 73–194 eV panels in Figures 3(a) (STEREO A) and Figure 3(b) (STEREO B) generally reflects the PAD features seen in the 58–121 eV WIND energy channels in Figure 2 with a corresponding short time-shift. STEREO PAD patterns in the 246.6 eV channel (the middle PAD panels of Figure 3) are consistent with WIND 255 eV PAD in Figure 2 in which the formation of a sunward-directed strahl stripe can be observed. The highest-energy 650.7 eV STEREO PAD in Figure 3 is completely different from the other PADs. It shows signatures of intermittent bidirectionality, following the location of MIs and CSs, very similar to the lower-energy PADs of WIND (Figure 2), especially in the region with the largest MIs and the local density increase (see Figure 3(b)).

Note that the IMF variations observed by the three spacecraft do not coincide with each other since the size of plasmoids produced by the fragmented swirl at 1 au is too small, and the direction of propagation is too radial to trace each MI with the three spacecraft. The size of MIs observed by STEREO A (Figure 3(a)) is generally smaller than that observed by WIND and STEREO B, which is understandable because the main part of the swirl with the smallest-size flux ropes was directed toward the STEREO A position. At the same time, the behavior of the total IMF observed by STEREO B is rather similar to that seen at L1 because STEREO B is closer to WIND than STEREO A.

### 3. Simulation of Local Acceleration of Electrons Observed in the Solar Wind: Interpretation of Observed PAD Features

#### 3.1. Main Features of Particle Acceleration in 3D RCSs

In order to understand the PAD features discussed above and to test the idea about the existence of locally borne suprathermal electrons, we show key results of simulations of

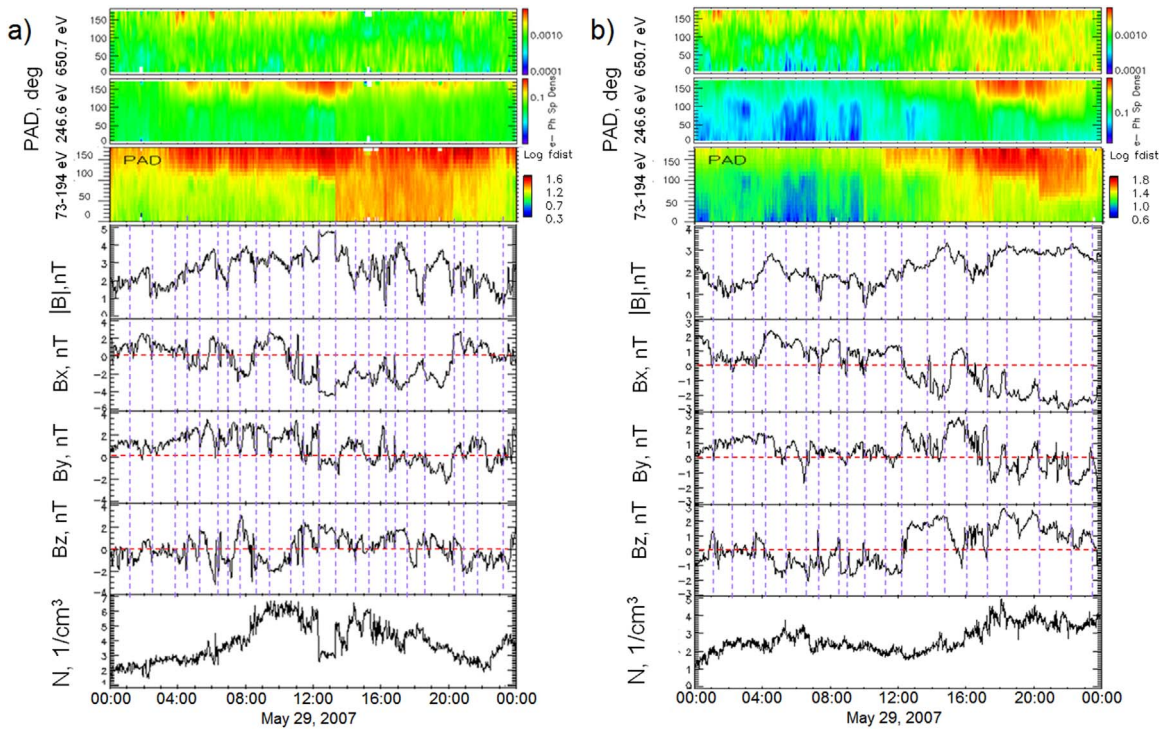


**Figure 3.** Analogous to Figure 2, but for STEREO A (a) and STEREO B (b). Upper PAD panels are for the 650.7, 246.6, and 73–194 eV energy channels.

the properties of electrons accelerated in typical RCS and MI configurations, considering the ambient plasma feedback to the presence of accelerated particles discussed in Xia & Zharkova (2020).

We trace particles in the vicinity of a 3D current sheet with a half-width of one gyroradius ( $d = 1.0\rho_i$  along  $X$ ) extended along  $Z$ .  $B$  is the static magnetic field induced by magnetic reconnection.  $B_0$  is the maximal magnitude of the magnetic field, and the reconnection electric field  $E_y$  accelerating particles is perpendicular to the reconnection plane. Particles from the ambient neutral plasma are dragged into the reconnection region from both sides by the magnetic diffusion process, leaving the RCS only after those gain the critical energy required to break from the magnetic field topology shown in Figure 4(a) (see details in Zharkova & Gordovskyy 2005; Xia & Zharkova 2018, 2020). After that, particles with opposite charges (electrons versus protons/ions) are ejected into the opposite semiplanes. Particles of the same charge form two distinct groups (“transit” and “bounced”) with very different energies and trajectories (Figure 4(a)). The maximal energy reached by each population depends on  $B_y$ . (Siversky & Zharkova 2009; Xia & Zharkova 2018). If  $B_y/B_0$  varies from 0 to 1, bounced electrons (lower-energy electrons, bottom panels in Figure 4(b)) can be accelerated to energies with the upper threshold from 20 eV to 500 eV, respectively, while transit electrons gain energies approaching hundreds of kiloelectron volts (higher-energy electrons, upper panels in Figure 4(b)).

Figure 4(b) shows that the two populations behave very differently, forming different PAD patterns, which are sensitive to  $B_y$  and  $d$ . PADs of electrons accelerated in CSs without the guide field  $B_y/B_0 = 0$  are quite symmetric with respect to the midplane, but when  $B_y$  increases, asymmetry increases respectively.

### 3.2. Spatial and Energy Distributions of Energetic Electrons in MIs

If dynamical MIs occur in an RCS, even more complex PADs compared to those shown in Figure 4(b) can be observed. Xia & Zharkova (2020) modeled particle acceleration in squashed (contracting) and coalescent (merging) MIs formed in RCSs. The model of a current sheet with multiple X- and O-nullpoints (MIs) is adopted from Kliem (1994) and described in detail by Xia & Zharkova (2020). Here we show an example of a PAD observed by a virtual spacecraft crossing the system of two merging MIs and CSs surrounding them (Figure 5). A complex PAD with a clear signature of bidirectionality is observed within the MIs in the higher-energy channel (the same feature is seen in squashed MIs in a narrower area centered in the middle of an MI—not shown). At the same time, at edges of dynamical MIs, PAD patterns may vary from dispersionless to completely defocused. Lower-energy electrons do not leave MIs showing the most intense PAD profiles at their edges.

### 3.3. Interpretation of the Observed Pad Features in RCSs and MIs

PADs of electrons observed in realistic plasmas containing numerous X-nullpoints and MIs are far more complex than the simulations provided above because the final picture formed by accelerated particles is determined by the magnetic field topology and the reconnection rate, which depend on the magnitude of the guide field, the dimension of RCSs and MIs, and the plasma density. Nonetheless, knowing that all the effects are cumulative, some of the key points of Figures 2 and 3 can be easily understood from Figures 4(b) and 5.

The electrons in the upper left PAD of Figure 4(b) are ejected mainly along  $0^\circ$ – $180^\circ$ , and the RCS midplane is clearly visible as a vertical stripe. This PAD pattern is often observed

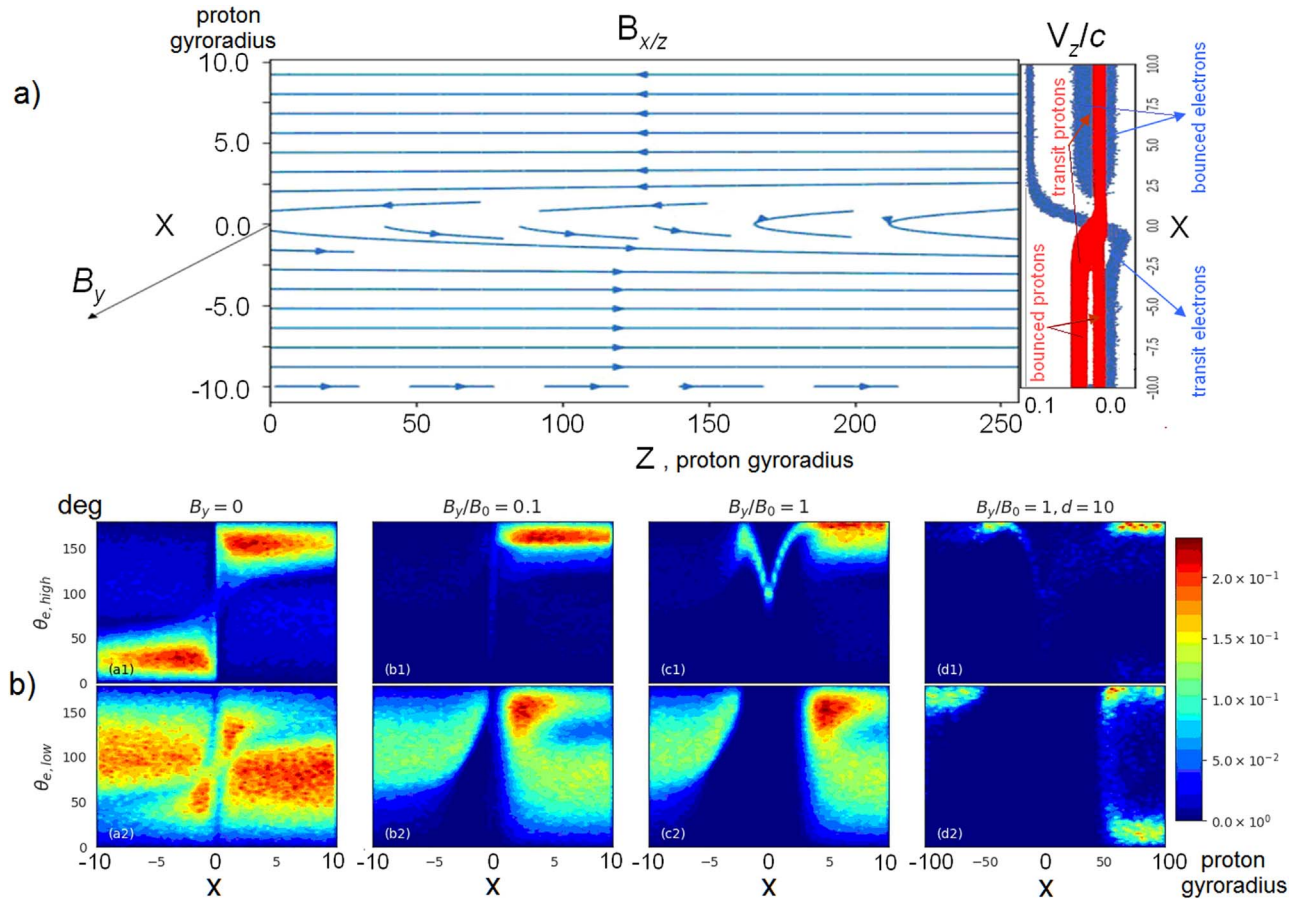


**Figure 4.** Model of the acceleration of solar wind electrons to suprathermal energies at the 3D RCS. (a) Topology of magnetic field lines in the vicinity of the single X-null point of the RCS (on the left), and example of 2.5D particle-in-cell simulations (3D by velocity  $V$  and 2D by coordinate) of particle trajectories for the strong guide field,  $B_y/B_0 = 1$  (on the right). Bounced particles form clouds at the injection side with respect to the midplane, but more energetic transit particles are ejected into the opposite semiplane. (b) PADs for electrons with lower energy (bottom row) and higher energy (top row) for the guide field  $B_y$  of different strength:  $B_y/B_0 = 0$  (first column, weak guide field), 0.1 (second column), and 1.0 (third column, strong guide field). RCS width  $d = 1.0 \rho_i$  (thin RCS) in the three columns ( $B_0 = 10^{-9}$  T). The fourth column is given for comparison under the conditions of thicker RCS and strong guide field ( $B_y/B_0 = 1$ ,  $d = 10 \rho_i$ ).

in the solar wind (see Figures 2 and 3) but has always been interpreted in terms of crossing of the HCS or a similar current sheet connected to the solar source. This study shows that such a pattern just reflects a crossing of a single thin current sheet reconnecting in a weak guide field.

A bird-like pattern especially clearly seen in the middle of the right panel of Figure 3 and in Channel 9 of Figure 2 indicates a crossing of the CS reconnecting in a strong guide field. According to Figure 4(b), it is not expected to be seen in lower-energy channels.

Figures 4(b) and 5 suggest that an intense unidirectional PAD stripe is formed in the areas with bigger MIs (Figures 2 and 3) because electrons can be accelerated to higher energies in bigger MIs, propagating much further from the initial acceleration sites (X-nullpoints or MI pools) and gradually becoming strahls that mix with solar origin strahls and contribute to the total PAD picture in the middle- and higher-energy channels.

Counterstreaming electrons appear naturally in the lower energy channel of Figure 4(b) when the guide field is rather strong, and a huge dropout encompassing the midplane is seen in the three bottom panels (lower-energy electrons) and the top-right panel (higher-energy electrons, strong  $B_y$ , and the wide RCS). Finding this important PAD feature easily solves the mystery of the observation of numerous narrow dropouts

associated with CSs in the solar wind. PAD simulations presented in Figure 4(b) allow us to suggest that the occurrence of dropouts and their properties are mainly determined by the width of RCSs and the reconnection rate.

Figure 5 also shows a clear signature of bidirectionality of higher-energy strahl electrons trapped and reaccelerated in dynamical MIs, while lower-energy electron paths are less structured. Wide dropouts are seen mainly in Figure 5 in the area free of merging MIs. It is noteworthy that bidirectionality and dropouts in PADs can be observed in the cases of both relatively low and high energies. Therefore, such PAD features can be determined by properties of a particular RCS or MI region of any origin.

The lower-energy PAD in Figure 2 (the lower color panel) shows the rotation of the direction of the electron flux in the area of dynamic MIs separated by CSs. Figure 5 suggests that this is the case when lower-energy electrons cannot leave dynamical MIs and trace the local IMF topology.

One more specific point is that, according to simulations, lower- and higher-energy electrons produce differently appearing PADs, which suggests that such a difference observed in higher- and lower energy PAD channels is a signature of local particle acceleration.

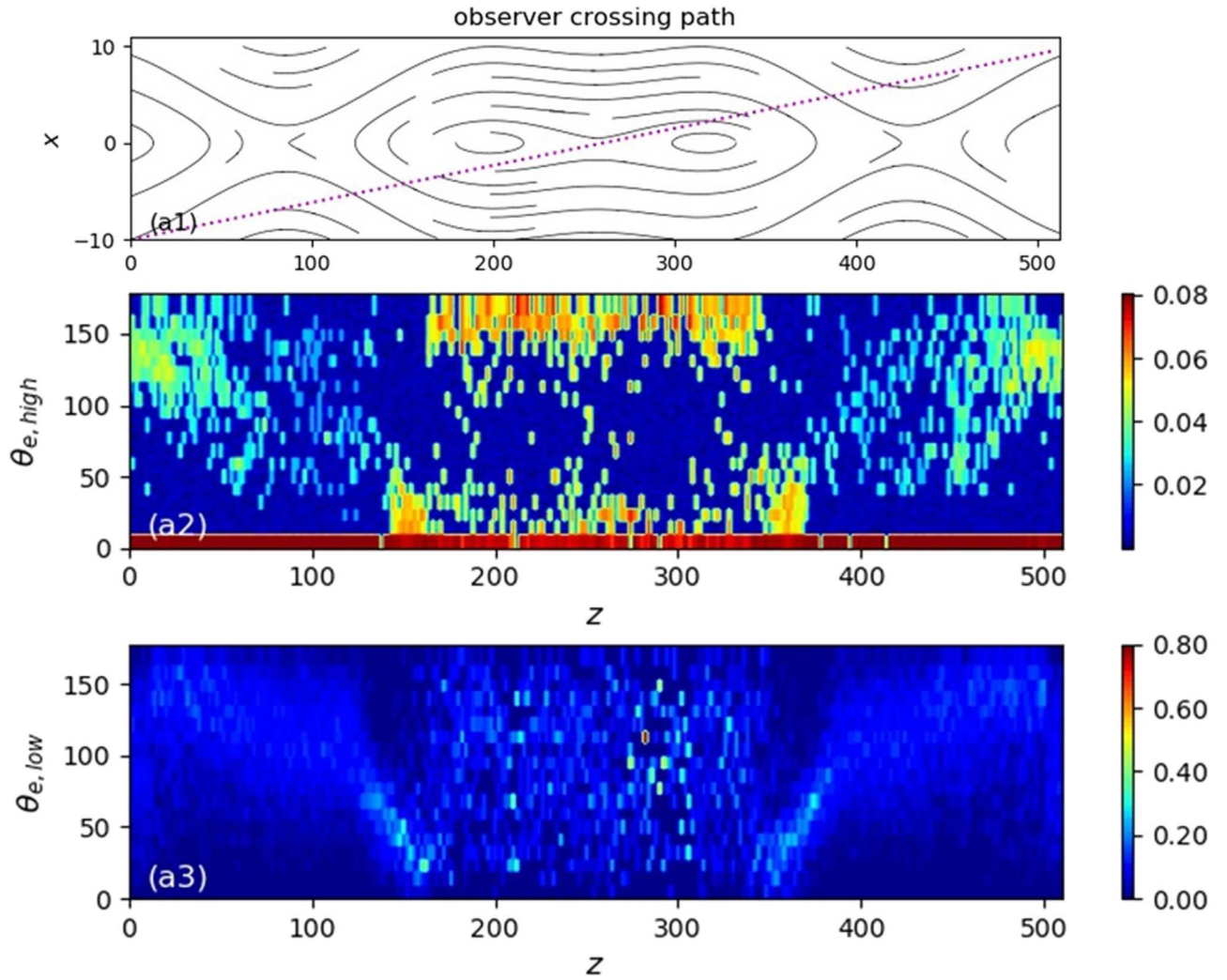


**Figure 5.** PADs observed when a hypothetical spacecraft crosses two coalescent MIs. The top plot presents the magnetic field topology (black lines) and the paths of a spacecraft (purple line). Middle and bottom color plots present the PADs of higher (middle) and lower (bottom) energy electrons accelerated in the system of the islands and CSs. Parameters of the islands employed are  $B_0 = 10^{-9}$  T,  $E_0 = 0.100$  mV m $^{-1}$ ,  $B_y/B_0 = 0.1$ ,  $d = 2\rho_i$ ,  $k = L/d = 0.0325$ .  $L$  is the half length of the island,  $d$  is the current sheet half-thickness. Both counterstreaming strahls and dropouts may be observed in such a configuration.

#### 4. Summary

We present multispacecraft observations of suprathermal electron PADs at  $\sim 1$  au that cannot be easily interpreted within the classical paradigm that all suprathermal electrons originate in the solar corona. We suggest that suprathermal electrons accelerated locally in the solar wind are mixed up with the well-known population of electrons of solar origin. Using PIC simulations, we show that key PAD features such as (i) heat flux dropouts and vertical PAD stripes encompassing RCSs, (ii) bidirectionality of strahls, and (iii) dramatically different PAD patterns observed in different energy channels can be explained by the behavior of electrons accelerated up to hundreds of electron volts directly in the solar wind while thermal particles pass through local RCSs and/or dynamical 3D plasmoids (or 2D MIs).

Resulting PAD views strongly depend on properties of particular RCSs, MIs, plasma/IMF parameters, and the magnetic topology. In the most complex cases, one can expect to see the solely solar-originating electrons in the highest-energy channels unaffected by local processes (e.g., Malandraki et al. 2002, 2003, 2005), and the lower- and middle-

energy channels in PADs provide important information on the local magnetic topology and features of ongoing magnetic reconnection in the observed plasma sample. Although there have been studies of the complex energy-dependent behavior of suprathermal electrons accelerated in the systems comprising CSs and MIs/flux ropes (Egedal et al. 2015; Du et al. 2018; Li et al. 2019; Lazarian et al. 2020), an application of simulated PAD features to observations has never been implemented before.

Importantly, since the solar wind-borne population of suprathermal electrons contributes to the total number of halo and strahl electrons, it can impact the halo/strahl relative density radial dependence and lead to the still unexplained increase of their isotropization with distance (Štverák et al. 2009; Graham et al. 2017; Horaites et al. 2019) because the role of solar wind-borne strahls decreases at large heliocentric distances owing to the decreasing density, weakening magnetic field, and reconnection rate.

The same approach can be used to explain a significant and not well-understood radial dependence of the relative density of warm and hot populations of suprathermal electrons associated with comets. We support the idea that the hot population is

formed by accelerated core electrons (Myllys et al. 2019), and suggest that the source of the acceleration is magnetic reconnection at strong CSs in cometary comas, including those observed in the Churyumov–Gerasimenko comet (Volwerk et al. 2017). If so, the observed radial dependence again represents a natural consequence of the weaker CSs and less efficient strahl production at larger heliocentric distances.

Summarizing our findings, we can conclude that acceleration of core electrons to suprathermal energies is a universal process that occurs in various systems associated with CSs and dynamical MIs in different plasmas. Therefore, related investigations of the solar wind should not be restricted by the paradigm of suprathermal electrons solely originating from the solar corona. The current study clearly highlights the importance of previously poorly investigated effects of local particle acceleration and may be useful to a broad community of space plasma researchers.

The Solar Electron and Proton Telescope STEREO data were obtained from <http://www2.physik.uni-kiel.de/STEREO/index.php> (thanks to B. Heber and A. Klassen). HET data are from [http://www.srl.caltech.edu/STEREO/Public/HET\\_public.html](http://www.srl.caltech.edu/STEREO/Public/HET_public.html) (thanks to A. Davis and T. von Rosenvinge), and other STEREO data were provided by the STEREO science center: <https://stereo.nascom.nasa.gov/data.shtml>. The Wind and ACE public data are from [https://cdaweb.gsfc.nasa.gov/istp\\_public/](https://cdaweb.gsfc.nasa.gov/istp_public/) (thanks to the CDAWeb team). O.K. is supported by RSCF grant No. 20-42-04418. V. Z. and Q.X. acknowledge the funding for this research provided by the U.S. Air Force, grant PRJ02156. The simulations used the DiRAC Complexity system, operated by the University of Leicester IT Services, which forms part of the STFC DiRAC HPC Facility ([www.dirac.ac.uk](http://www.dirac.ac.uk)). This equipment is funded by BIS National E-Infrastructure capital grant ST/K000373/1 and STFC DiRAC Operations grant ST/K0003259/1. DiRAC is part of the UK National e-Infrastructure.

### ORCID iDs

O. Khabarova  <https://orcid.org/0000-0002-3230-2033>  
 V. Zharkova  <https://orcid.org/0000-0002-8608-1280>  
 Q. Xia  <https://orcid.org/0000-0001-8717-1360>  
 O. E. Malandraki  <https://orcid.org/0000-0002-4751-6835>

### References

- Adhikari, L., Khabarova, O., Zank, G. P., & Zhao, L.-L. 2019, *ApJ*, **873**, 72  
 Anderson, B. R., Skoug, R. M., Steinberg, J. T., & McComas, D. J. 2012, *JGRA*, **117**, A04107  
 Crooker, N. U., Kahler, S. W., Larson, D. E., & Lin, R. P. 2004, *JGRA*, **109**, A03108  
 Crooker, N. U., & Pagel, C. 2008, *JGRA*, **113**, A02106  
 Drake, J., Cassak, P., Shay, M., Swisdak, M., & Quataert, E. 2009, *ApJL*, **700**, L16  
 Du, S., Guo, F., Zank, G. P., Li, X., & Stanier, A. 2018, *ApJ*, **867**, 16  
 Egedal, J., Daughton, W., Le, A., & Borg, A. L. 2015, *PhPI*, **22**, 101208  
 Eyink, G. L. 2015, *ApJ*, **807**, 137  
 Foullon, C., Lavraud, B., Wardle, N. C., et al. 2009, *SoPh*, **259**, 389  
 Gómez-Herrero, R., Malandraki, O., Dresing, N., et al. 2011, *JASTP*, **73**, 551  
 Gosling, J. T., Baker, D. N., Bame, S. J., et al. 1987, *JGR*, **92**, 8519  
 Gosling, J. T., McComas, D. J., Skoug, R. M., & Smith, C. W. 2006, *GeoRL*, **33**, L17102  
 Graham, G. A., Rae, I. J., Owen, C. J., et al. 2017, *JGRA*, **122**, 3858  
 Horaites, K., Boldyrev, S., & Medvedev, M. V. 2019, *MNRAS*, **484**, 2474  
 Kajdič, P., Blanco-Cano, X., Opitz, A., et al. 2013, in AIP Conf. Proc. 1539, Proc. Thirteenth Int. Solar Wind Conf.: Solar Wind 13, ed. G. P. Zank et al. (Melville, NY: AIP), 203  
 Khabarova, O., Zank, G. P., Li, G., et al. 2015, *ApJ*, **808**, 181  
 Khabarova, O., Zank, G. P., Li, G., et al. 2016, *ApJ*, **827**, 122  
 Khabarova, Olga V., & Zank, Gary P. 2017, *ApJ*, **843**, 4  
 Khabarova, O. V., Malandraki, O. E., Zank, G. P., et al. 2018, in Proc. IAU Symp. 335, Space Weather in the Heliosphere: Processes and Forecasts, ed. C. Foullon & O. Malandraki (Cambridge: Cambridge Univ. Press), 76  
 Kliem, B. 1994, *ApJS*, **90**, 719  
 Lazarian, A., Eyink, G. L., Jafari, A., et al. 2020, *PhPI*, **27**, 012305  
 Le Roux, J. A., Webb, G. M., Khabarova, O. V., Zhao, L.-L., & Adhikari, L. 2019, *ApJ*, **887**, 77  
 le Roux, J. A., Zank, G. P., & Khabarova, O. V. 2018, *ApJ*, **864**, 158  
 le Roux, J. A., Zank, G. P., Webb, G. M., & Khabarova, O. 2015, *ApJ*, **801**, 112  
 le Roux, J. A., Zank, G. P., Webb, G. M., & Khabarova, O. V. 2016, *ApJ*, **827**, 47  
 Li, X., Guo, F., Li, H., Stanier, A., & Kilian, P. 2019, *ApJ*, **884**, 118  
 Malandraki, O., Khabarova, O., Bruno, R., et al. 2019, *ApJ*, **881**, 116  
 Malandraki, O. E., Lario, D., Lanzerotti, L. J., et al. 2005, *JGRA*, **110**, A09S06  
 Malandraki, O. E., Sarris, E. T., Lanzerotti, L. J., et al. 2002, *JASTP*, **64**, 517  
 Malandraki, O. E., Sarris, E. T., & Tsiropoula, G. 2003, *AnGeo*, **21**, 1249  
 Matthaeus, W. H., Ambrosiano, J. J., & Goldstein, M. L. 1984, *PhRvL*, **53**, 1449  
 McComas, D. J., Gosling, J. T., Phillips, J. L., et al. 1989, *JGR*, **94**, 6907  
 Mingalev, O. V., Khabarova, O. V., Malova, K. V., et al. 2019, *SoSysR*, **53**, 30  
 Myllys, M., Henri, P., Galand, M., et al. 2019, *A&A*, **630**, A42  
 Owens, M. J., Crooker, N. U., & Lockwood, M. 2013, *JGRA*, **118**, 1868  
 Pagel, C., Crooker, N. U., Larson, D. E., Kahler, S. W., & Owens, M. J. 2005, *JGRA*, **110**, A01103  
 Rouillard, A. P., Lavraud, B., Davies, J. A., et al. 2010, *JGRA*, **115**, A04104  
 Simunac, K. D. C., Galvin, A. B., Farrugia, C. J., et al. 2012, *SoPh*, **281**, 423  
 Siversky, T. V., & Zharkova, V. V. 2009, *JPIPh*, **75**, 619  
 Štverák, Š., Maksimovic, M., Trávníček, P. M., et al. 2009, *JGRA*, **114**, A05104  
 Uzdensky, D. A., & Loureiro, N. F. 2016, *PhRvL*, **116**, 105003  
 Vocks, C., Salem, C., Lin, R. P., & Mann, G. 2005, *ApJ*, **627**, 540  
 Volwerk, M., Jones, G. H., Broiles, T., et al. 2017, *JGRA*, **122**, 3308  
 Xia, Q., & Zharkova, V. 2018, *A&A*, **620**, A121  
 Xia, Q., & Zharkova, V. 2020, *A&A*, **635**, A116  
 Zank, G. P., Hunana, P., Mostafavi, P., et al. 2015, *ApJ*, **814**, 137  
 Zank, G. P., le Roux, J. A., Webb, G. M., Dosch, A., & Khabarova, O. 2014, *ApJ*, **797**, 28  
 Zharkova, V., & Khabarova, O. 2012, *ApJ*, **752**, 35  
 Zharkova, V., & Khabarova, O. 2015, *AnGeo*, **33**, 457  
 Zharkova, V. V., & Gordovskyy, M. 2005, *SSRv*, **121**, 165